Mahar *et al. Energy Mater.* **2025**, *5*, 500049
DOI: 10.20517/energymater.2024.111

Energy Materials

Article

Open Access

Check for updates

High performance, low-cost rechargeable aluminum ion battery using Nb_2CTx-MoS_2 composite cathode

Nasurullah Mahar[1], Tawfik Abdo Saleh[1], Amir Al-Ahmed[1,2,*], Abdulaziz A. Al-Saadi[1,3,*]

[1]Department of Chemistry, King Fahd University of Petroleum & Minerals, Dhahran 31261 Saudi Arabia.
[2]Interdisciplinary Research Center for Sustainable Energy Systems (SES), King Fahd University of Petroleum & Minerals, Dhahran 31261, Saudi Arabia.
[3]Interdisciplinary Research Center for Refining and Advanced Chemicals, King Fahd University of Petroleum & Minerals, Dhahran 31261, Saudi Arabia.

***Correspondence to:** Dr. Amir Al-Ahmed, Interdisciplinary Research Center for Sustainable Energy Systems (SES), King Fahd University of Petroleum & Minerals, Dhahran 31261, Saudi Arabia. E-mail: aalahmed@kfupm.edu.sa; Dr. Abdulaziz A. Al-Saadi, Interdisciplinary Research Center for Refining and Advanced Chemicals, King Fahd University of Petroleum & Minerals, Dhahran 31261, Saudi Arabia. E-mail: asaadi@kfupm.edu.sa

How to cite this article: Mahar, N.; Abdo Saleh, T.; Al-Ahmed, A.; Al-Saadi, A. A. High performance, low-cost rechargeable aluminum ion battery using Nb_2CTx-MoS_2 composite cathode. *Energy Mater.* **2025**, *5*, 500049. https://dx.doi.org/10.20517/energymater.2024.111

Received: 6 Aug 2024 **First Decision:** 23 Oct 2024 **Revised:** 29 Oct 2024 **Accepted:** 14 Nov 2024 **Published:** 21 Feb 2025

Academic Editors: Sen Xin, Chengxin Li **Copy Editor:** Fangling Lan **Production Editor:** Fangling Lan

Abstract

Aluminum-ion batteries are among the promising low-cost researchable batteries with huge potential, due to their three-electron redox process, high theoretical capacity, and better safety compared to lithium-ion batteries. However, the reported capacity and cyclic stability still fall short of their theoretical values. This could be due to cathodic degradation, lattice distortion of working material, and anodic corrosion. To address these issues, Nb_2CTx-MoS_2 composite cathodes were fabricated using Nb_2CTx synthesized using the (HF-Free) green method and were further modified with MoS_2 by hydrothermal process. Pouch cell (2 × 2 inches) was assembled employing Nb_2CTx-MoS_2 composite as a cathode and aluminum film (0.01 mm) as an anode in $AlCl_3$/[BMIm]Cl (1.5) ionic liquid electrolyte. The modified cathode showed a specific capacity of ~350 mAh/g at a current density of 100 mA/g. The cell was able to retain nearly 98% of its coulombic efficiency after 500 cycles.

Keywords: Aluminum-ion battery, composite cathode, specific capacity, coulombic efficiency

INTRODUCTION

The growing demand for safe and cost-effective energy storage devices is the driving force for efforts on different battery technologies. Conventional lithium-ion batteries have revolutionized energy storage technology and have been used as a major power source in portable electronics and even in electric vehicles. It has been proven to be a key energy storage device in the preceding decade with several shortcomings, such as safety, higher prices, and limited reserves[1,2]. In recent times, aluminum-ion batteries (AIBs) have been getting significant attention due to their lower cost (3rd most abundant element in the Earth's crust)[3] and environmental safety. Additionally, AIBs have an extraordinary theoretical volumetric capacity of 8,056 mAh/cm^3 driven by its three-electron redox process[4,5]. Over the past two decades, significant efforts have been made to improve the cathode of the AIBs for both aqueous and non-aqueous electrolyte systems[6]. However, one of the main limitations that persists for the purely aqueous system is its relatively narrow electrochemical stability window along with the anodic corrosion[7,8]. Ionic liquid electrolytes (ILEs) showed promise to overcome some of these limitations. The electrolyte enhanced stability and ionic conductivity, while offering a wider electrochemical window, improved thermal stability and reduced volatility. Despite all these advantages, ILEs have a few disadvantages as well, such as the higher viscosity of the ionic liquids, which can slow down ion transport, and high cost of some ILEs[7,8]. Nonetheless, the development of AIBs operating at room temperature remained elusive until the utilization of chloroaluminate-based ILEs[9]. Cells prepared with ILEs, such as amide-based electrolytes, demonstrated superior efficiency, capacity, and cyclic and high-voltage stability[7,10]. Moreover, working with ILEs provides the benefit of wide electrochemical windows, good ionic conductivity, and thermal stability, rendering them ideal candidates for AIBs[10-12]. Recent research found that the molten ILE, such as 1-Ethyl 3-methylimidazolium chloride (EMIm]Cl), can significantly improve the performance of AIBs[13]. The presence of chloroaluminate anions $[AlxCly]_n^-$ (including $AlCl_4^-$, $Al_2Cl_7^-$, and $Al_3Cl_{10}^-$) plays a critical role in reversible Al^{3+}/Al electrochemistry with an excellent coulombic efficiency (CE)[10,14]. The intercalation/deintercalation of these complex anions triggers structural deformities and lattice distortions in the cathode due to the large effective radius of anions, resulting in irreversibility and rapid capacity decay[15]. This emphasizes a critical challenge that must be addressed to achieve better performance and long-term stability. Innovations are advancing energy density, cycling stability, and minimizing corrosion and dendrites through electrolyte additives and surface coatings[6]. Current directions include hybrid battery systems, in-depth SEI layer characterization, and eco-friendly recycling methods. With the abundance and recyclability of aluminum, AIBs are well-positioned to be sustainable, high-performance energy storage solutions in the future[16].

A cathode with wide interlayer space to accommodate complex aluminum ions is required which would subsequently overcome the storage and lattice distortion challenges[17,18]. To address these challenges, multilayered structures such as iron chalcogenides hybrid cathodes (FeS_2@C[19], $NiCo_2S_4$[20], and MoS_2/C[21]) were fabricated. The metal sulfur polar bond facilitated formation of the Al-Cl bond and reduced the electrostatic interactions during the charge/discharge process[22-25]. Subsequently, it is also essential to build suitable electrodes with weak coulombic contact and a sturdy framework capable of housing the intercalated complex ions without considerable structural change following the galvanostatic charge-discharge (GCD) process. MXenes, known for their inspiring electrochemical properties, wide interlayer space, high conductivity, surface area, and tunable surface chemistry, have been proven to be an efficient cathode material for AIBs[26,27]. Among the various MXenes, Niobium carbide (Nb_2CTx) has better thermodynamic, kinetic and oxidative stability and poses better aggregation resilience. Due to these characteristics, the Nb_2CTx poses a better discharge voltage plateau compared to that of Ti and V-based MXenes[28].

In this work, the highly conductive, wide interlayer space characteristics of Nb_2CTx and the pseudo-capacitive behavior of the MoS_2 were exploited to improve electrochemical kinetics, enabling rapid charge-discharge rates and high stability. Nb_2CTx enhances the overall conductivity of the cathode, facilitating faster ion movement within the electrode and improving the battery's rate capability[29]. Conversely, MoS_2 can act as a buffer material, controlling large volume changes during ion intercalation and deintercalation within the cathode. This buffering effect can help improve the cycling stability of the AIB[30]. This unique combination of Nb_2CTx and MoS_2 supported by the green synthesis (HF-free etchant) of the Nb_2CTx and $AlCl_3$/[BMIM]Cl as an ionic liquid-based system has not been reported previously. Thus, Nb_2CTx was prepared using $FeCl_3$ as a green etchant in the presence of complexing agents. Meanwhile, triethylamine (TEA) was used for stabilizing its interlayer spacing and further modified with MoS_2 to obtain a modified composite for the AIB cathode. For comparison, an AIB cell with pure Nb_2CTx as a cathode was also prepared and tested. The pouch cell (2 × 2 inches) was fabricated using a cathode (Nb_2CTx-MoS_2 and Nb_2CTx), aluminum metal anode, and $AlCl_3$:[BMIm]Cl as electrolyte [Supplementary Figure 1]. Detailed assembly and electrolyte preparation are discussed in the Supplementary Material. The composite cathode-based AIBs exhibited a discharge capacity of 350 mAh/g over 500 cycles at a current density of 100 mA/g. This performance significantly surpassed that of bare Nb_2CTx cathode-based AIBs and other reported cells [Supplementary Table 1].

CHEMICALS AND MATERIALS

Nb_2AlC MAX phase precursors, iron(III) chloride ($FeCl_3$, 48%-54%), and TEA were purchased from Alfa Aesar. Anhydrous aluminum chloride (99.99%), 1-butyl-3-methylimidazolium chloride (98.0%), and aluminum foil of 0.01 mm thickness (99.99%) were purchased from Sigma-Aldrich. The carbon paper, Celgard 2500 monolayer polypropylene (PP) membrane of 16 μm thickness, and aluminum laminated film were purchased from the local supplier. All the chemicals and reagents were consumed without additional purification.

Instrumentation

The synthesized Nb_2CTx and its composite Nb_2CTx-MoS_2 were characterized by Field Emission scanning electron microscopy (FE-SEM: Zeiss Merlin), high-resolution transmission electron microscopy (HR-TEM), X-ray diffraction (XRD: Bruker D8 Advance), Raman spectroscopy, and X-ray photoelectron spectroscopy (XPS: Amicus). Electrochemical studies such as cyclic voltammetry (CV), and impedance of the cell were recorded using a Gamry (Reference 3000) while the GCD was conducted using 8-channel battery analyzers BTS8-5V5A. XPS was used to analyze the interactions of cathode material with intercalated ions. After 500 consecutive cycles, the Nb_2CTx-MoS_2 cathode was removed from the cell, carefully cleaned with acetone, dried, and characterized by XRD, Raman spectroscopy, and XPS to study the structural changes that occurred during cycling.

Synthesis of MXenes and composite cathode

Nb_2CTx MXenes were synthesized by following a HF-free green approach from Nb_2AlC precursors by modifying a reported method[31]. In a typical wet etching process, a solution of $FeCl_3$ 0.1 M and tartaric acid as a complexing agent (1.2 M) was prepared in a closed Teflon bottle over an ice bath. Then, 2 g of Nb_2CTx was slowly mixed into this cold solution with constant stirring at 300 rpm for 10 min. The mixture was transferred over an oil bath (in an inert environment to avoid early oxidation) at 35 °C for 24 h. The product was washed several times with an ethanol-water (1:1) mixture until natural pH was obtained. Subsequently, Nb_2CT_x was intercalated with 20% TEA at room temperature for 3 h. The dispersed Nb_2CTx flakes were washed with an ethanol-water (1:1) mixture by centrifuging, followed by sonication for 10 min. The supernatant was collected each time until the transparent solution was observed.

Likewise, the Nb_2CTx-MoS_2 composite was prepared by a hydrothermal method. In a modified approach, 4.8 g of $Na_2MoO_4 \cdot 2H_2O$ and the required amount of thiourea were dissolved in 50 mL deionized water (DIW) with continuous stirring, followed by the addition of 76 mg of Nb_2CTx dispersed in 3 mL of poly (dimethyldiallylammonium chloride) (PDDMAC) (20%). To maintain the pH of the solution at 6.5, the required amount of HCl was added. The mixture was then transferred into a Teflon-lined stainless-steel autoclave and heated at 180 C for 24 h. The black-colored powder was washed several times to remove all impurities. Finally, the composite was dried in a vacuum oven and annealed at 400 C under constant Argon flow. Various concentrations and ratios of the respective salts were tested, and the above procedure yielded better results; hence, it was selected for further study. The overall synthesis process has been presented schematically in Figure 1.

RESULTS AND DISCUSSION

To investigate the structure and morphology, Nb_2CTx and composite Nb_2CTx-MoS_2 were studied through various instrumental techniques, including XRD, FE-SEM, HR-TEM, XPS, and Raman spectroscopy. XRD patterns of exfoliated few-layer Nb_2CTx can be seen in Figure 2A. The figure shows the characteristic peak (002) of Nb_2CTx has shifted to 2θ angle of 6.97°, compared to multilayered M-Nb_2CTx at 9.46° and the precursor [Supplementary Figure 2] MAX phase (13.92°) after etching. This shift of basal plane (002) indicates an increase in the d-spacing to 4.27 nm (calculated by Braggs equation) after the etching of the aluminum layer and intercalation. These patterns are in line with the (PDF #30-0033) for the hexagonal phase Nb_2C of space-group P63/mmc[29]. Figure 2B displays the hybrid diffraction patterns of the composite Nb_2CTx-MoS_2. Here, all characteristic peaks of Nb_2CTx and MoS_2 are visible, with slight shifts in peak position and changes in intensity; for instance, the Nb_2CTx peak 6.97° has moved to a smaller angle of 6.44° compared to pure Nb_2CTx[30]. Additionally, a new wide band emerges at 15.67° signifying the successful incorporation of MoS_2. Likewise, the diffraction patterns observed at 19.12°, 22.74°, 32.19°, and 49.32° agree well with the literature[30]. Moreover, non-basal-plane peaks, such as (004), (103), and (106) at 13.92°, 36.12°, and 42.21°, respectively, have either eroded or experienced a decrease in intensity. These observations suggest structural modifications induced by the incorporation of MoS_2 and intercalation processes.

The layered morphology of the Nb_2CTx is shown in the FE-SEM image [Figure 2C]. A few-layered accordion-like structure of Nb_2CTx reflects the successful engraving of Al. Likewise, Figure 2D shows the FE-SEM images of the Nb_2CTx-MoS_2 composite; the substantial change in morphology with small flower-like crystallites of MoS_2 covering the Nb_2CTx flakes is observed, which confirms the formation of a well-defined composite and is assumed to enhance the conductivity and surface area of an electrode[32]. Figure 2E shows the HR-TEM images of the Nb_2CTx transparent sheets and accordion-like shape due to the chemical etching of the Al atomic layers showing the few-layered arrangements of the as-prepared Nb_2CTx. Similarly, Figure 2F shows the selected area diffraction (SAED) image; the diffraction rings demonstrate the (100), (102), (421) and (002) planes of the Nb_2CTx crystals. Supplementary Figure 3A-C shows the Raman, TEM images for the prepared composite. Supplementary Figure 3B reveals clear lattice fringes associated with the Nb_2CTx component. The measured interplanar d-spacing of the material was found to be approximately 4.27 nm. This value corresponds to a specific crystal plane within the Nb_2CTx structure, providing information about its crystallinity. Besides, the TEM images offer direct visualization of the layered structure characteristic of both Nb_2CTx and MoS_2, as both materials consist of sheets or flakes stacked upon one another. In Supplementary Figure 3C, the individual layers of the Nb_2CTx-MoS_2 can be distinguished, appearing as relatively large, transparent regions. Their transparency in the TEM micrograph is due to the ultrathin nature of the Nb_2CTx flakes. The presence of MoS_2 in the composite is indicated by two features: Some of the observed transparent flakes may also be individual MoS_2 sheets, depending on their orientation and thickness. Similarly, for Nb_2CTx, the layered structure and very thin flakes can appear transparent

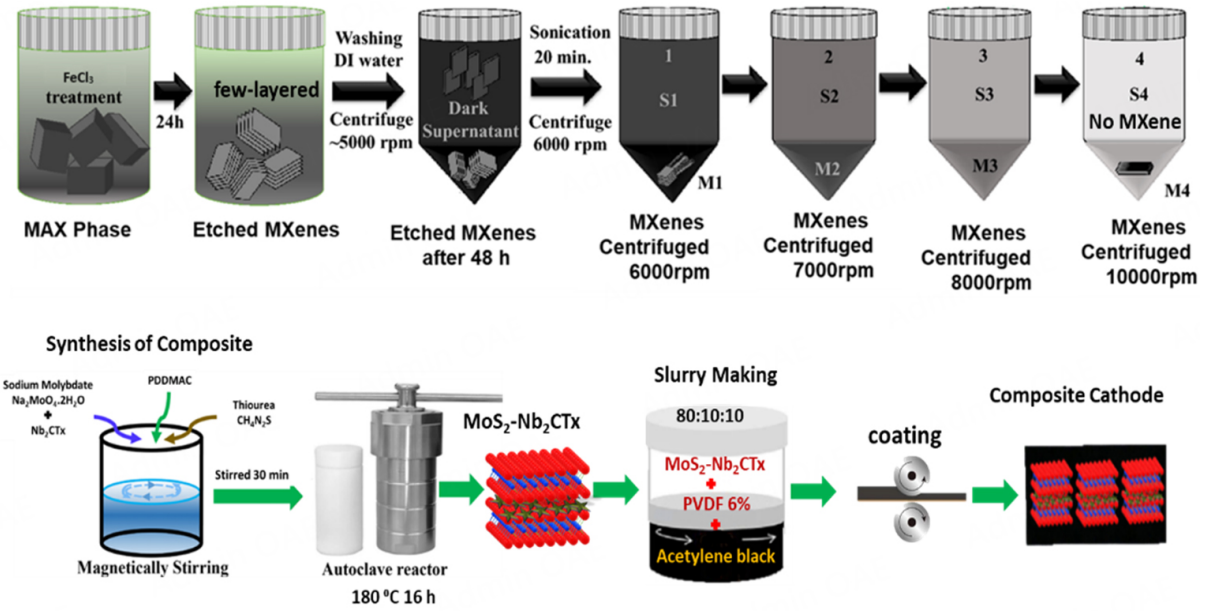

Figure 1. Schematic representation of synthesis of Nb_2CTx by green etchant ($FeCl_3$ + TA). Synthesis of Nb_2CTx-MoS_2 composites by hydrothermal method. Additionally, the preparation of slurry with 80:10:10 ratio of active material, conducting carbon and PVDF binder respectively followed by pasting slurry on carbon paper is depicted.

under TEM. More prominently, the presence of MoS_2 is evident as dark, irregularly shaped patches overlying the Nb_2CTx flakes. These darker regions correspond to thick MoS_2 sheets deposited on the surface of the Nb_2CTx. The contrast difference between Nb_2CTx and MoS_2 allows for their visual distinction in the TEM image.

Figure 3A shows *ex-situ* XRD patterns for free and composite electrodes after successive ten and 500 charge/discharge cycles. A change in the XRD pattern is observed after the GCD process with the appearance of new peaks at 36.01°, 32.19°, and a rise in intensity for the pattern at 32.19° indicates the intercalation of ions during charge and discharge cycles in the cathode. These outcomes are in good agreement with the reported literature[33,34]. This was further confirmed by the Raman spectroscopy [Figure 3B] and energy dispersive X-ray spectroscopy (EDS) characterization [Supplementary Figure 4]. Figure 3B shows the Raman peaks located at 157, 191, 327, and 425 cm^{-1} ascribed to $Al_2Cl_7^-$ and $AlCl_4^-$ ions accordingly; a noticeable shift in band position and change in intensities (i.e., 157, 191, 327, and 425 cm^{-1} to 152, 194, 330 and 418 cm^{-1}) after the 500 cycles have been observed, indicating ion intercalation. Additionally, Supplementary Figure 3A represents the Raman spectra Nb_2CTx-MoS_2 and Nb_2CTx. In the spectrum of Nb_2CTx, there are two broad peaks at 1,435 and 1,477 cm^{-1}, which correspond to the D and G modes characteristic of carbon species. Additionally, a broad peak at 700-800 cm^{-1} is likely due to the presence of Nb-Tx (Terminals -OH, -O, -Cl) bonds. Similarly, the peak at 162 and at 218 cm^{-1}, which slightly shifts from the original 173 and 201 cm^{-1}, corresponds to the A_1g and E_2g mode vibrations from the in and out-of-plane movements of Nb and C atoms, confirming the layered structure of Nb_2CTx. Likewise, in the Raman spectrum of $Nb_2CTx@MoS_2$, the D and G bands are reduced, indicating an interaction between Nb_2CTx and MoS_2, while two sharp peaks at 318 and 418 cm^{-1} correspond to the E_2g and A_1g modes of MoS_2, respectively. This again confirms the successful intercalation of complex ions and matches well with the previously reported Raman spectra[35]. Figure 3C shows the *ex-situ* SEM images for the Nb_2CTx-MoS_2 after the first ten GCD cycles. The cracks on the electrode surface gesture the impact of ion intercalation and deintercalation on the cathode. Similarly, Figure 3D presents SEM images after the 500 charging-discharging cycles, where the appearance of the

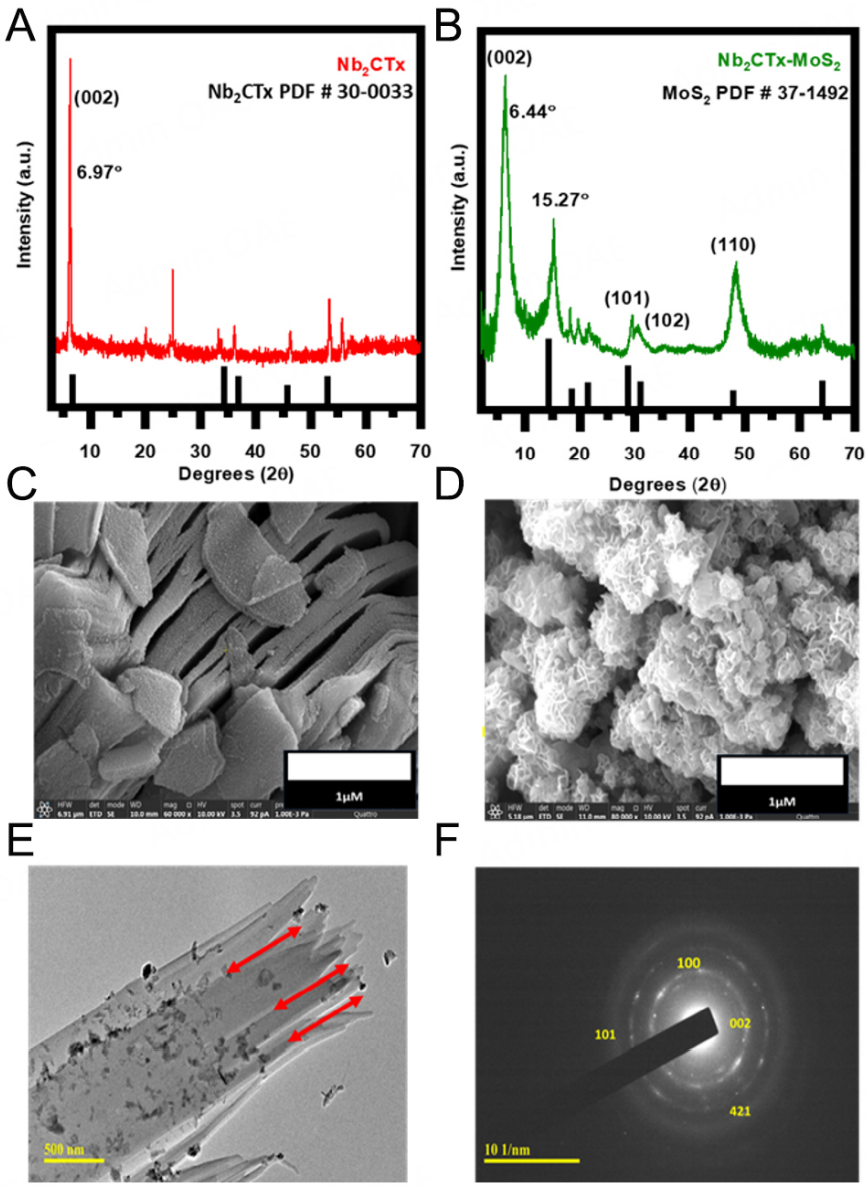

Figure 2. Morphological and structural characterization of as-prepared Nb_2CTx and its composite (A) XRD patterns of few layered Nb_2CTx, (B) XRD patterns for the Nb_2CTx-MoS_2 composite, (C) FE-SEM images of Nb_2CTx showing the layered structure, (D) FE-SEM images of the composite after the loading of MoS_2 with change in morphology, (E) HR-TEM images of the Nb_2CTX flakes showing well-scattered layers, (F) SAED image of the spot where TEM was conducted.

buds-like growth on the surface of the cathode pits suggests the long intercalation and deintercalation during the cycling study; however, the basic layered structure remains intact with no significant structural degradation.

Supplementary Figure 5 presents the survey XPS analysis of Nb_2CTx-MoS_2, revealing the presence of Mo, S, Nb, C, and terminations resulting from the mild etching technique. To delve deeper into the anticipated operating mechanism, surface electronic states, and chemical composition, XPS tests were conducted on the electrode pre- and post-charging/discharge cycles. Figure 4A-C showcases the XPS spectra of the Nb 3d core levels of Nb_2CTx-MoS_2 before and after charging. Notably, during full charge, the binding energy of the

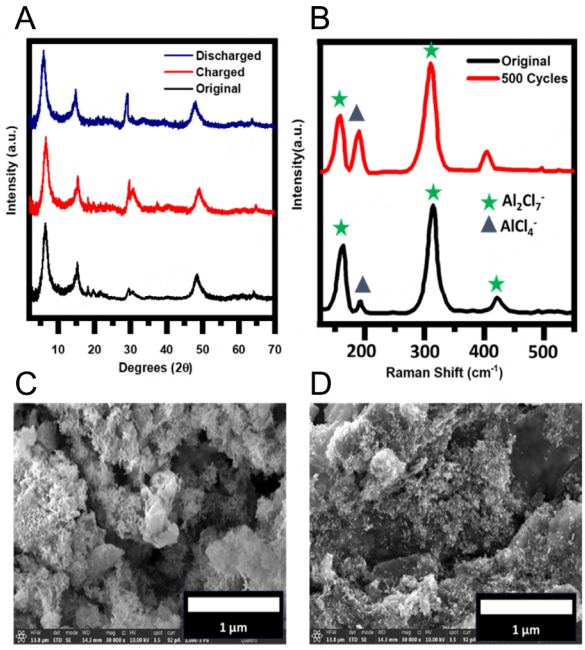

Figure 3. The structural analysis and morphology of cathode after the charge-discharge process (A) *Ex-situ* XRD patterns for composite cathode after 10th and 500th charge/discharge cycles, (B) Raman spectra of the cathode at the 10th and after 500th cycle showing the changes in electrolyte chemistry, (C) FE-SEM images represent the cathode morphology after 500 cycles, (D) shows the high-resolution FE-SEM images after 500th cycle.

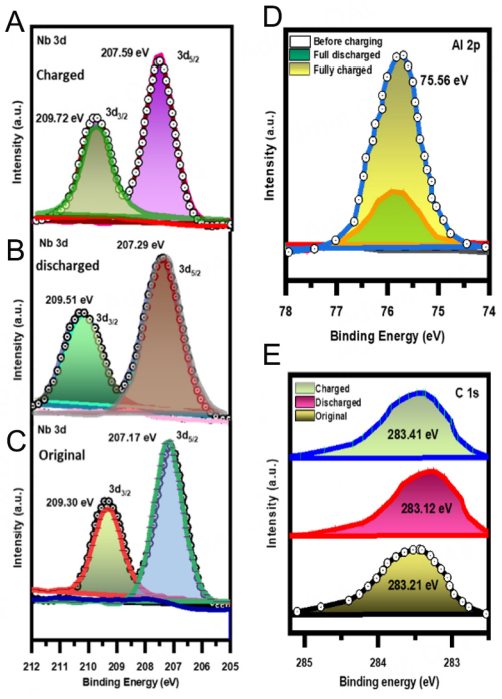

Figure 4. The XPS spectra depicting the change in position of binding energy of the major elements of the composite cathode before and after GCD process (A) XPS peaks for the Nb 3d core at fully charged state, (B) after discharging, (C) original composite cathode before GCD, (D) XPS peaks for the Al 2p at before charging, discharged, and fully charged stages, (E) XPS peaks for carbon in all three stages of original to charged.

Nb 3d core increased from 207.17 (Original) to 207.59 eV after fully charged, indicative of redox chemistry between the cathode surface and the intercalated ions[30]. Figure 4D and E elucidates changes in the XPS core levels of Al 2p and C 1s, respectively.

Prior to GCD, minimal peaks are visible for Al 2p, suggesting a sparse presence of these elements. However, post-charging, a notable augmentation in Al 2p XPS peaks (at 75.56 and 199.56 eV, respectively) underscores the pronounced intercalation of $[AlCl_4]^-$ ions within the cathode [Figure 4D]. This heightened intensity provides convincing evidence of successful ion intercalation. Similarly, upon full discharge, a noticeable reduction in both Al 2p signals signifies the substantial deintercalation of $[AlCl_4]^-$ ions from the cathode. Additionally, a noticeable increase in binding energies (from 283.21 to 283.41 eV) in the C 1s spectra following charging/discharging sequences [Figure 4E] confirms the observed chemisorption phenomena between the cathode and embedded ions[30]. These observations collectively illustrate the interaction between electrode components and embedded ions during charge-discharge cycles, offering valuable insights into modifications in surface chemistry and the electrochemical behavior of the system[36].

Electrochemical study

The performance of bare and composite cathodes was evaluated by performing CV and electrochemical impedance spectroscopy (EIS) using Biologic VMP3 multichannel Potentiostat, while the GCD was conducted using 8-channel battery analyzers BTS8-5V5A; the cut-off voltage (upper/lower) was set as 2.8/0.5 V accordingly and all the electrochemical measurements were taken at room temperature. Figure 5 displays the CV and GCD curves of the bare Nb_2CTx and Nb_2CTx-MoS_2 composite cathodes in an optimized 1.5 ratio of $AlCl_3$/[BMIm]Cl electrolyte (details in Supplementary Material). Figure 5A depicts the CV responses of Nb_2CTx cathodes recorded between the potential window of 0.5 to 2.7 V *vs.* Al^{3+}/Al at a sweep rate of 0.1 mVs^{-1}. It shows two anodic peaks of around 1.7-1.8 V (I) and 2.4-2.5 V (II), whereas the two cathodic peaks are at 2.2-2.1 V (III) and 1.6-1.5 V (IV), respectively. Likewise, Figure 5B displays CV curves for the composite cathode Nb_2CTx-MoS_2 and carbon paper at similar conditions. These complimentary anodic/cathodic peaks show the two-step electrochemical reaction between composite cathodes and Al which could be linked to aluminum ion intercalation and deintercalation at two different positions on the cathode; this behavior is well aligned with previous reports[37-39]. Significant changes have been observed at anodic peaks such as a shift in position and increase in current has been observed at 1.9-2.1 V (I) and 2.3-2.4 V (II); likewise, a change in the cathodic curve has also been witnessed with a wide band at 1.9-1.7 V (III) and 2.4-2.2 V (IV). Conversely, the two cathodic peaks during the negative sweep (reduction) could correspond to the multi-step insertion of aluminum ions back into the cathode structure. This might involve a stepwise reduction process of the previously oxidized material. This indicates the increased reversible ion intercalation on respective electrodes. The increase in the anodic peak current reflects that the electrode intercalates more electroactive species in the double layer (the layer in close proximity to the working electrode) and, therefore, more charge transfer at that potential which indicated that the current intensity has been maximized.

The charge/discharge cycles of the bare Nb_2CTx cathode [Figure 5C] were evaluated at various current densities extending from 10-300 mA/g. It has been observed that by varying the current densities as 10, 50, 100, and 300 mA/g, the charge/discharge capacity drops quickly with an increase in the current densities. In addition, it can be observed from Figure 5C that the charge/discharge plateaus split progressively and grow with the rise in the current density, which is due to the increased polarization, sluggish diffusion of complex ions through the Nb_2CTx structure. It resulted in not only slow charge/discharge rates but also poor cycle stability. Likewise, Figure 5D depicts the charge/discharge curves of the cell with Nb_2CTx-MoS_2 cathodes at current densities of 10, 50, 100, and 300 mA/g. The specific capacities were observed to be 510, 400, 350, and 290 mAh/g, respectively, for the current densities of 10, 50, 100, and 300 mA/g. A comparatively slow decay

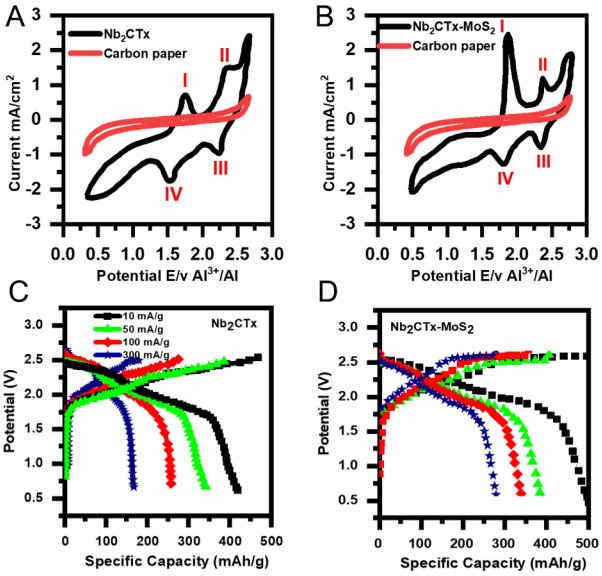

Figure 5. Cyclic voltammetry and GCD curves at different current densities for both electrodes (A) CV curve for the bare Nb_2CTx at scan rate of 0.1 mV s^{-1} and carbon paper, (B) charge/discharge curves of Nb_2CTx at current densities ranging from 10-300 mA/g specific capacity, (C) CV curves of Nb_2CTx-MoS_2 and carbon paper at 0.1 mV s^{-1}, (D) charge/discharge curves of Nb_2CTx-MoS_2 at current densities ranging from 10-300 mA/g.

and close specific capacities compared to bare Nb_2CTx were observed. Similarly, in Figure 5D, the two charge plateaus are observed between 2.16-2.43 and 2.49-2.52 V, while the discharge plateaus are located around 2.5-2.43 and 2.10-1.89 V accordingly at a current density of 100 mA/g. It is evident that the composite cathode can maintain a capacity of 350 mAh/g after 50 to 500 cycles [Figure 6], which is much greater than the bare Nb_2CTx cathode with better cycle stability. The slight variation in charge cut-offs is due to the effect of current densities on the electrochemical performance of the battery. At higher current densities, the battery experiences increased polarization and resistance, which can affect the charge-discharge voltage profile and lead to an earlier charge cut-off to avoid overcharging[40]. By contrast, at lower current densities, the system experiences less polarization, allowing for a more gradual and complete charging process, which can result in a slightly higher charge cut-off[41]. This approach ensures that the cell operates within safe limits across various current densities while optimizing performance.

The cycle stability and corresponding CE of AIBs were examined at a current density of 100 mA/g. Figure 6A portrays the cyclic stability and CE of the Nb_2CTx cathode over 500 cycles. Initially, the Nb_2CTx cathode boasted an impressive capacity of 400 mAh/g. However, after just 50 cycles, an abrupt decline resulted, with the capacity plateauing at 250 mAh/g over the subsequent 500 cycles at a steady current density of 100 mA/g. The accompanying CE, documented in Figure 6C, remained suboptimal at 83%. This trend may be attributed to coulombic interactions between the chloroaluminate ions and the strong electronegative terminals inherent in the Nb_2CTx electrode materials[38]. Conversely, Figure 6B offers insight into the cycle stability of the modified Nb_2CTx-MoS_2 cathode over the same 500-cycle period at a 100 mA/g current density. Notably, the GCD curves remained remarkably consistent and stable throughout the duration of the test. Although exhibiting a similar trend during the initial 50 cycles, the modified cathode displayed a notably higher initial capacity of approximately 550 mAh/g, which gradually decayed at a slower pace compared to its Nb_2CTx counterpart. The observed enhancement in cyclic stability and capacity retention of the composite cathode can be attributed to the incorporation of MoS_2, which likely suppressed undesirable coulombic interactions. Likewise, the kinetic advantages of using Nb_2CT_x-MoS_2 as a composite

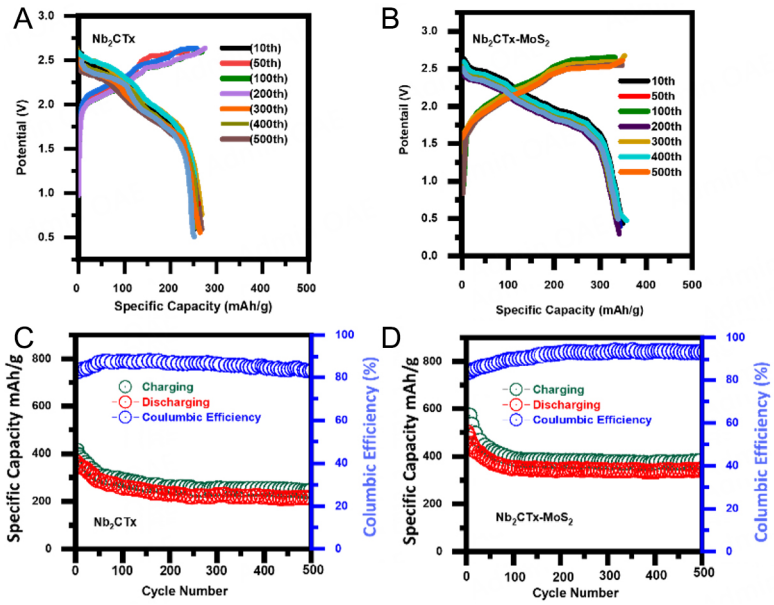

Figure 6. Specific capacity of both electrodes for 500 cycles and corresponding coulombic efficiency of the cathodes for 500 GCD cycles (A) Long-term GCD curves and specific capacity of Nb_2CTx at 100 mA/g current density, (B) long-term GCD curves and specific capacity of Nb_2CTx-MoS_2 at 100 mA/g current densities, (C) coulombic efficiency and cyclic performance of Nb_2CTx at 100 mA/g, (D) Coulombic efficiency and cyclic performance for the Nb_2CTx-MoS_2 composite cathode at 100 mA/g.

cathode stem from its enhanced ionic conductivity, improved charge transfer characteristics, increased active reaction sites, favorable intercalation dynamics, and thermal stability. These factors contribute to faster kinetics, higher specific capacities, and improved overall performance of AIBs. In addition, the pseudocapacitive behavior of the MoS_2 facilities rapid and reversible redox reactions with aluminum ions[30]. Besides, the combination of high surface area, pseudocapacitive behavior, electrical conductivity, synergistic effects, and structural stability of Nb_2CTx-MoS_2 composite cathode contributes to the excellent enhancement of specific capacity. This indicates that the Nb_2CTx-MoS_2 is more stable than the pure Nb_2CTx cathode, overcoming the structural deformity and columbic forces. This can be attributed to the presence and synergic effect of MoS_2 and eventually improved the reversibility of the composite electrode[30,42]. The composite electrode-based cell was able to maintain the charge-discharge plateaus at 500 cycles indicating stable reversibility. The composite cathode has shown outstanding cycling stability with the retention of nearly 98% of its initial capacity of 350 mAh/g at a current density of 100 mA/g even after 500 cycles [Figure 6D]. Slight increase in CE over cycling can be attributed to the gradual stabilization of the solid electrolyte interphase (SEI) layer[43]. As during the very initial cycles, SEI layers can form and stabilize, which consumes some of the active ions and results in slightly lower CE. However, as cycling progresses, the SEI layer becomes more uniform and passivated, which minimizes further ion consumption and thus improved the CE[38]. Additionally, following the GCD cycling process, the cell components were inspected again to confirm the absence of corrosion, thus making the ILEs a top choice of electrolyte for AIBs to obtain long cycle life and stability.

To further evaluate the electrochemical performance of the Nb_2CTx-MoS_2 cathode, EIS study was conducted on both bare and composite Nb_2CTx-MoS_2 cathodes across the frequency range of 10^5 to 10 Hz. Nyquist plots of the Nb_2CTx-MoS_2 composite and Nb_2CTx bare electrodes at 10, 50, 100, and 200 cycles are shown in Figure 7A and B. The open circuit potential of the Nb_2CTx-MoS_2 cathode-based cell was measured at approximately 2.68 V [Figure 7C]. Notably, the inset showcases the successful powering of a 1.8 V red light-emitting diode (LED) lamp for 40 h, underscoring the practical utility of the battery. The fitting results

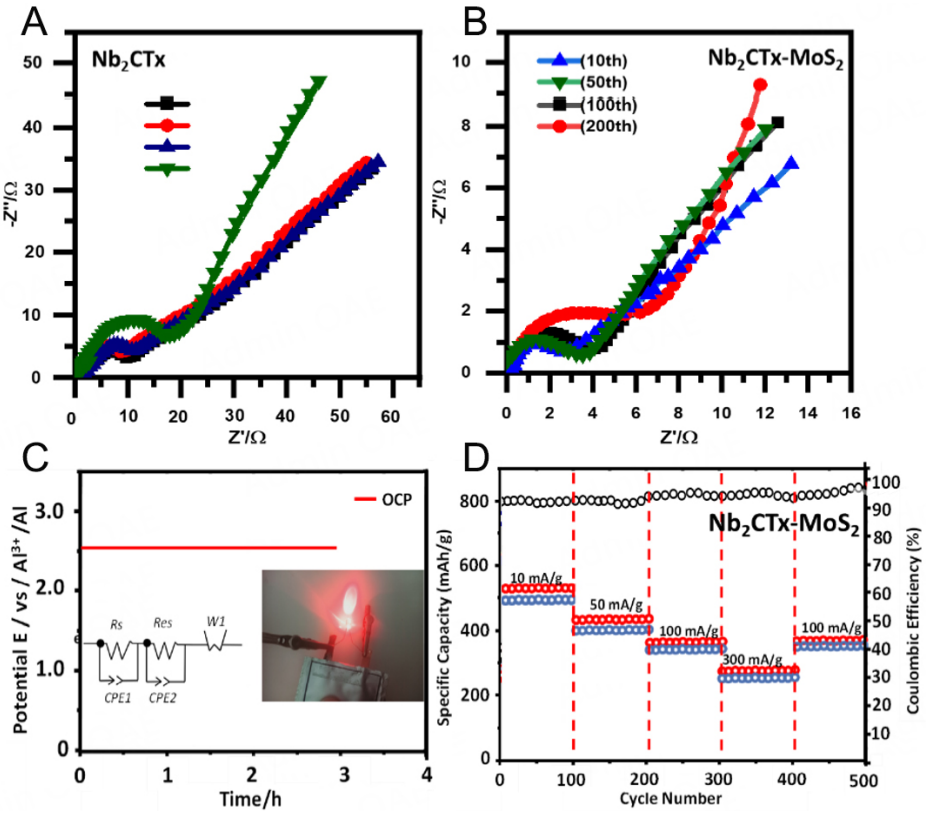

Figure 7. (A) Nyquist plots of Nb_2CTx at different cycles, (B) Nyquist plots of Nb_2CTx-MoS_2 composite at 10, 50, 100, and 200th cycles, (C) Open circuit potential and the equivalent circuit model of the pouch cell, (D) rate capability and coulombic efficiency of Nb_2CTx-MoS_2 performed at varying current densities extending from 10 to 300 mA/g for 500 cycles.

for the equivalent circuit model of the modified cathode material revealed Rs and Rct values of 10.12 and 3.81 Ω for the composite and bare electrodes, respectively. Remarkably, the charge transfer resistance of the modified cathode material was determined to be 6.45 Ω, substantially lower than that of the bare Nb_2CTx cathode material (21.4 Ω) after 200 cycles, and this trend is similar to that of previously reported work[44]. This improved Rct value is attributed to the integration of MoS_2, which positively enhanced the overall conductivity and structural integrity of the composite. Supplementary Figure 6A-C depicts the LED lamp's operation over 0, 20, and 40 h, respectively, following full charging. The rate capabilities of the fabricated AIB based on the Nb_2CTx-MoS_2 cathode battery were assessed across different current densities ranging from 10 to 300 mA/g over 100 cycles [Figure 7D]. Although the discharge capacity exhibited a decline with increasing current density, it notably rebounded to 350 mAh/g with a columbic efficiency of 98% upon reducing the current density back to 100 mA/g. This behavior emphasizes the stability and reversibility of the composite cathode, suggesting promising prospects for its practical application.

Intercalation study

Figure 8 shows the schematic intercalating/de-intercalating process of $AlCl_4^-$, Cl^- and Al^{3+} ions at the cathode during the charge/discharge process. The $AlCl_4^-$ was observed to be the key ion for the electrochemistry of batteries. The $AlCl_3$/[BMIm]Cl ILE comprises two key anionic species at room temperature ($AlCl_4^-$ and $Al_2Cl_7^-$)[45]. The molar ratio of ILE was established as 1.5 to ensure a high concentration of $[Al_2Cl_7]^-$ and low pH, which favors the reversible accumulation and dissolution of aluminum metal on the electrodes. During the charging process, the $AlCl_4^-$ ions are intercalated into cathode Nb_2CTx-MoS_2 interlayers and an electron is released (I). At the anode, free electron is accepted by $Al_2Cl_7^-$, which results in $AlCl_4^-$ and Al which deposit

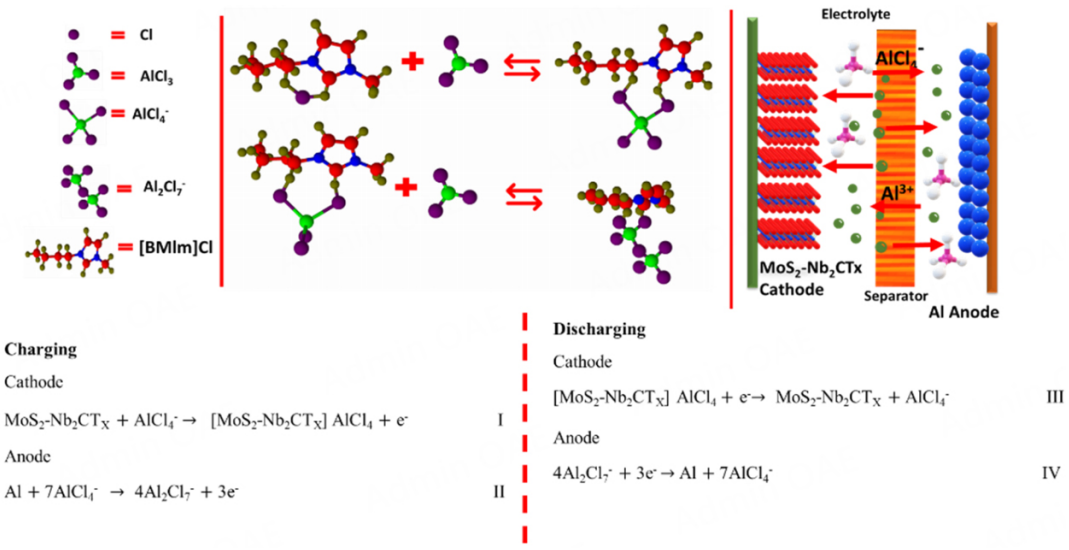

Figure 8. Optimized structure of the respective ions, overall chemistry of electrolyte and complex ion formation, the model battery operation where the ions flow to respective electrodes during the charge and discharge process is observed and the ion intercalation/deintercalation during the charge-discharge process at the cathode and anode.

on anode (II). During the discharge process, the $AlCl_4^-$ is deintercalated from the cathode (III), while at the anode, the Al reacts with $AlCl_4^-$ anions, thus producing $Al_2Cl_7^-$, and three electrons are liberated (V), thus disturbing the concentration balance of anions in the electrolyte[43,46]. The proposed charge/discharge mechanism is well aligned with the CV response, where the anodic peak at 1.9-2.1 V (I) and 2.3-2.4 V (II) with increased current corresponds to the intercalation of anions and transformation of $Al_2Cl_7^-$; similarly, a change in the cathodic curve has also been witnessed with a wide band at 1.9-1.7 V (III) and 2.4-2.2 V (IV) [Figure 5B]. This indicates the increased reversible intercalation of ions during the charge/discharge process on respective electrodes[47-49]. Consequently, the Nb_2CTx-MoS_2 composite cathode offers a significant improvement of performance of the AIB with better efficiency compared to previously reported (capacity of 250 mAh/g)[29], thus addressing some key challenges (specific capacity, kinetics, and structural stability). The unique synergy of the Nb_2CTx MXene and MoS_2 into the composite structure holds great promise for advancing the development of high-performance and cost-effective AIBs.

CONCLUSION

For the first time, the Nb_2CTx was synthesized by HF-free green etchants and transformed into a Nb_2CTx-MoS_2 composite cathode to obtain a unique syngeneic combination to improve the performance of the AIB. The developed composite (Nb_2CTx-MoS_2) cathode showed a high capacity of 350 mAh/g, and good cycle life, which is significantly higher than previously reported AIBs. The XRD, XPS, and FE-SEM images confirmed the successful fabrication of the Nb_2CTx-MoS_2 composite with enhanced electrochemical characteristics. The AIB was subjected to 500 charge/discharge cycles at the current density of 100 mA/g and was able to retain nearly 98% of its CE. The XPS findings demonstrated the successful intercalation and deintercalation of the $AlCl_4^-$ anion ions in cathode layered structure with a significant change in binding energies; hence, a better capacity and cycle life were obtained. Furthermore, the improved electrochemical performance of Nb_2CTx-MoS_2 cathodes is attributed to good interlayer spacing, electrical conductivity and stability of the MXene, and further the synergistic effect after MoS_2 deposition. This composition reduced weak coulombic interaction, enhanced surface area, and improved conductivity, which were responsible for the improved battery performance.

DECLARATIONS

Authors' contributions

Methodology, investigation, formal analysis, data curation, writing - original draft: Mahar, N.
Methodology, supervision, writing - review & editing: Abdo Saleh, T.
Concept, visualization, writing - original draft, writing - review & editing: Al-Ahmed, A.
Conceptualization, methodology, supervision, writing - review & editing, project administration, funding acquisition: Al-Saadi, A. A.

Availability of data and materials

Data and materials are available and can be obtained by contacting the corresponding author.

Financial support and sponsorship

The authors gratefully acknowledge the funding from the King Fahd University of Petroleum & Minerals (KFUPM), Saudi Arabia, through grant (PAES-2400).

Conflicts of interest

All authors declared that there are no conflicts of interest.

Ethical approval and consent to participate

Not applicable.

Consent for publication

Not applicable.

REFERENCES

1. Chayambuka, K.; Mulder, G.; Danilov, D. L.; Notten, P. H. L. From Li-ion batteries toward Na-ion chemistries: challenges and opportunities. *Adv. Energy. Mater.* **2020**, *10*, 2001310. DOI
2. Fan, E.; Li, L.; Wang, Z.; et al. Sustainable recycling technology for Li-ion batteries and beyond: challenges and future prospects. *Chem. Rev.* **2020**, *120*, 7020-63. DOI
3. Zhou, Q.; Zheng, Y.; Wang, D.; et al. Cathode materials in non-aqueous aluminum-ion batteries: progress and challenges. *Ceram. Int.* **2020**, *46*, 26454-65. DOI
4. Ponnada, S.; Kiai, M. S.; Krishnapriya, R.; Singhal, R.; Sharma, R. K. Lithium-free batteries: needs and challenges. *Energy. Fuels.* **2022**, *36*, 6013-26. DOI
5. Nayem SM, Ahmad A, Shaheen Shah S, Saeed Alzahrani A, Saleh Ahammad AJ, Aziz MA. High performance and long-cycle life rechargeable aluminum ion battery: recent progress, perspectives and challenges. *Chem. Record.* **2022**, *22*, e202200181. DOI
6. Ma, D.; Li, J.; Li, H.; et al. Progress of advanced cathode materials of rechargeable aluminum-ion batteries. *Energy. Mater. Adv.* **2024**, *5*, 0088. DOI
7. Raić, M.; Lužanin, O.; Jerman, I.; Dominko, R.; Bitenc, J. Amide-based Al electrolytes and their application in Al metal anode-organic batteries. *J. Power. Sources.* **2024**, *624*, 235575. DOI
8. Wu, Y.; Lin, W.; Tsai, T.; Lin, M. Unveiling the reaction mechanism of aluminum and its alloy anode in aqueous aluminum cells. *ACS. Appl. Energy. Mater.* **2024**, *7*, 3957-67. DOI
9. Wang, H.; Gu, S.; Bai, Y.; et al. Anion-effects on electrochemical properties of ionic liquid electrolytes for rechargeable aluminum batteries. *J. Mater. Chem. A.* **2015**, *3*, 22677-86. DOI
10. Macfarlane, D. R.; Forsyth, M.; Howlett, P. C.; et al. Ionic liquids and their solid-state analogues as materials for energy generation and storage. *Nat. Rev. Mater.* **2016**, *1*, 15005. DOI
11. Liu, T.; Vivek, J. P.; Zhao, E. W.; Lei, J.; Garcia-Araez, N.; Grey, C. P. Current challenges and routes forward for nonaqueous lithium-air batteries. *Chem. Rev.* **2020**, *120*, 6558-625. DOI PubMed
12. Hu, Y.; Fan, L.; Rao, A. M.; et al. Cyclic-anion salt for high-voltage stable potassium-metal batteries. *Natl. Sci. Rev.* **2022**, *9*, nwac134. DOI PubMed PMC
13. Ng, K. L.; Lu, Z.; Wang, Y.; Singh, C. V.; Azimi, G. Fundamental insights into electrical and transport properties of chloroaluminate

ionic liquids for aluminum-ion batteries. *J. Phys. Chem. C.* **2021**, *125*, 15145-54. DOI

14. Pastel, G. R.; Chen, Y.; Pollard, T. P.; et al. A sobering examination of the feasibility of aqueous aluminum batteries. *Energy. Environ. Sci.* **2022**, *15*, 2460-9. DOI
15. Jayaprakash, N.; Das, S. K.; Archer, L. A. The rechargeable aluminum-ion battery. *Chem. Commun.* **2011**, *47*, 12610. DOI PubMed
16. Zhang, Y.; Liu, S.; Ji, Y.; Ma, J.; Yu, H. Emerging nonaqueous aluminum-ion batteries: challenges, status, and perspectives. *Adv. Mater.* **2018**, *30*, e1706310. DOI
17. Ates, M.; Chebil, A.; Yoruk, O.; Dridi, C.; Turkyilmaz, M. Reliability of electrode materials for supercapacitors and batteries in energy storage applications: a review. *Ionics* **2022**, *28*, 27-52. DOI
18. Wang, S.; Kravchyk, K. V.; Pigeot-rémy, S.; et al. Anatase TiO_2 nanorods as cathode materials for aluminum-ion batteries. *ACS. Appl. Nano. Mater.* **2019**, *2*, 6428-35. DOI
19. Zhao, Z.; Hu, Z.; Jiao, R.; et al. Tailoring multi-layer architectured FeS_2@C hybrids for superior sodium-, potassium- and aluminum-ion storage. *Energy. Storage. Mater.* **2019**, *22*, 228-34. DOI
20. Li, S.; Tu, J.; Zhang, G. H.; Wang, M.; Jiao, S. $NiCo_2S_4$ nanosheet with hexagonal architectures as an advanced cathode for Al-ion batteries. *J. Electrochem. Soc.* **2018**, *165*, A3504. DOI
21. Yang, W.; Lu, H.; Cao, Y.; Xu, B.; Deng, Y.; Cai, W. Flexible free-standing MoS_2/carbon nanofibers composite cathode for rechargeable aluminum-ion batteries. *ACS. Sustain. Chem. Eng.* **2019**, *7*, 4861-7. DOI
22. Geng, L.; Scheifers, J. P.; Fu, C.; Zhang, J.; Fokwa, B. P. T.; Guo, J. Titanium sulfides as intercalation-type cathode materials for rechargeable aluminum batteries. *ACS. Appl. Mater. Interfaces.* **2017**, *9*, 21251-7. DOI
23. Xing, W.; Li, X.; Cai, T.; et al. Layered double hydroxides derived NiCo-sulfide as a cathode material for aluminum ion batteries. *Electrochim. Acta.* **2020**, *344*, 136174. DOI
24. Wang, S.; Jiao, S.; Wang, J.; et al. High-performance aluminum-ion battery with CuS@C microsphere composite cathode. *ACS. Nano.* **2017**, *11*, 469-77. DOI
25. Pan, W. D.; Liu, C.; Wang, M. Y.; et al. Non-aqueous Al-ion batteries: cathode materials and corresponding underlying ion storage mechanisms. *Rare. Metals.* **2022**, *41*, 762-74. DOI
26. Yuan, D.; Dou, Y.; Wu, Z.; et al. Atomically thin materials for next-generation rechargeable batteries. *Chem. Rev.* **2022**, *122*, 957-99. DOI
27. VahidMohammadi, A.; Hadjikhani, A.; Shahbazmohamadi, S.; Beidaghi, M. Two-dimensional vanadium carbide (MXene) as a high-capacity cathode material for rechargeable aluminum batteries. *ACS. Nano.* **2017**, *11*, 11135-44. DOI PubMed
28. Zhao, J.; Wen, J.; Bai, L.; et al. One-step synthesis of few-layer niobium carbide MXene as a promising anode material for high-rate lithium ion batteries. *Dalton. Trans.* **2019**, *48*, 14433-9. DOI
29. Li, J.; Zeng, F.; El-Demellawi, J. K.; et al. Nb_2CT_x MXene cathode for high-capacity rechargeable aluminum batteries with prolonged cycle lifetime. *ACS. Appl. Mater. Interfaces.* **2022**, *14*, 45254-62. DOI
30. Tan, B.; Lu, T.; Luo, W.; Chao, Z.; Dong, R.; Fan, J. A novel MoS_2-MXene composite cathode for aluminum-ion batteries. *Energy. Fuels.* **2021**, *35*, 12666-70. DOI
31. Mahar, N.; Al-ahmed, A.; Al-saadi, A. A. Synthesis of vanadium carbide MXene with improved inter-layer spacing for SERS-based quantification of anti-cancer drugs. *Appl. Surface. Sci.* **2023**, *607*, 155034. DOI
32. Ikram, M.; Raza, A.; Ali, S. 2D-materials for energy harvesting and storage applications. 2022. DOI
33. Yu, Z.; Tu, J.; Wang, C.; Jiao, S. A rechargeable Al/graphite battery based on $AlCl_3$/1-butyl-3-methylimidazolium chloride ionic liquid electrolyte. *ChemistrySelect* **2019**, *4*, 3018-24. DOI
34. Nahian, M. K.; Reddy, R. G. Electrical conductivity and species distribution of aluminum chloride and 1-butyl-3-methylimidazolium chloride ionic liquid electrolytes. *J. Phys. Org. Chem.* **2023**, *36*, e4549. DOI
35. Zheng, Y.; Dong, K.; Wang, Q.; Zhang, J.; Lu, X. Density, viscosity, and conductivity of lewis acidic 1-butyl- and 1-hydrogen-3-methylimidazolium chloroaluminate ionic liquids. *J. Chem. Eng. Data.* **2013**, *58*, 32-42. DOI
36. Chen, C.; Shi, M.; Zhao, Y.; Yang, C.; Zhao, L.; Yan, C. Al-Intercalated MnO_2 cathode with reversible phase transition for aqueous Zn-Ion batteries. *Chem. Eng. J.* **2021**, *422*, 130375. DOI
37. Yuan, Z.; Lin, Q.; Li, Y.; Han, W.; Wang, L. Effects of multiple ion reactions based on a $CoSe_2$/MXene cathode in aluminum-ion batteries. *Adv. Mater.* **2023**, *35*, e2211527. DOI
38. Angell, M.; Pan, C. J.; Rong, Y.; et al. High coulombic efficiency aluminum-ion battery using an $AlCl_3$-urea ionic liquid analog electrolyte. *Proc. Natl. Acad. Sci. USA.* **2017**, *114*, 834-9. DOI PubMed PMC
39. Xu, H.; Bai, T.; Chen, H.; et al. Low-cost $AlCl_3$/Et_3NHCl electrolyte for high-performance aluminum-ion battery. *Energy. Storage. Mater.* **2019**, *17*, 38-45. DOI
40. Seong, W. M.; Yoon, K.; Lee, M. H.; Jung, S.; Kang, K. Unveiling the intrinsic cycle reversibility of a $LiCoO_2$ electrode at 4.8-V cutoff voltage through subtractive surface modification for lithium-ion batteries. *Nano. Lett.* **2019**, *19*, 29-37. DOI
41. Nölle, R.; Beltrop, K.; Holtstiege, F.; Kasnatscheew, J.; Placke, T.; Winter, M. A reality check and tutorial on electrochemical characterization of battery cell materials: how to choose the appropriate cell setup. *Mater. Today.* **2020**, *32*, 131-46. DOI
42. Chen, C.; Xie, X.; Anasori, B.; et al. MoS_2-on-MXene heterostructures as highly reversible anode materials for lithium-ion batteries. *Angew. Chem. Int. Ed.* **2018**, *57*, 1846-50. DOI
43. Zhu, N.; Zhang, K.; Wu, F.; Bai, Y.; Wu, C. Ionic liquid-based electrolytes for aluminum/magnesium/sodium-ion batteries. *Energy. Mater. Adv.* **2021**, *2021*, 9204217. DOI

44. Li, Z.; Niu, B.; Liu, J.; Li, J.; Kang, F. Rechargeable aluminum-ion battery based on MoS_2 microsphere cathode. *ACS. Appl. Mater. Interfaces.* **2018**, *10*, 9451-9. DOI
45. Shen, X.; Sun, T.; Yang, L.; et al. Ultra-fast charging in aluminum-ion batteries: electric double layers on active anode. *Nat. Commun.* **2021**, *12*, 820. DOI PubMed PMC
46. Zheng, L.; Yang, H.; Bai, Y.; Wu, C. Multielectron reaction of $AlCl_n$ in borophene for rechargeable aluminum batteries. *Energy. Mater. Adv.* **2022**, *2022*, 0005. DOI
47. Pradhan, D.; Reddy, R. G. Mechanistic study of Al electrodeposition from EMIC-$AlCl_3$ and BMIC-$AlCl_3$ electrolytes at low temperature. *Mater. Chem. Phys.* **2014**, *143*, 564-9. DOI
48. Elterman, V.; Shevelin, P. Y.; Yolshina, L.; Borozdin, A. Features of aluminum electrodeposition from 1,3-dialkylimidazolium chloride chloroaluminate ionic liquids. *J. Mol. Liq.* **2022**, *351*, 118693. DOI
49. Shen, X.; Sun, T.; Wu, Z.; Tan, L. Ultrafast charging and ultralong cycle life in solid-state Al-ion batteries. *J. Mater. Chem. A.* **2022**, *10*, 8178-85. DOI